Carbon 171 (2021) 845–856

Contents lists available at ScienceDirect

Carbon

journal homepage: www.elsevier.com/locate/carbon

Research Article

High pressure high temperature synthesis of highly boron doped diamond microparticles and porous electrodes for electrochemical applications

Georgia F. Wood [a, b], Carmen E. Zvoriste-Walters [c], Mark G. Munday [c], Mark E. Newton [d], Viacheslav Shkirskiy [a], Patrick R. Unwin [a], Julie V. Macpherson [a, *]

[a] Department of Chemistry, University of Warwick, Coventry, United Kingdom
[b] Diamond Science and Technology Centre for Doctoral Training, University of Warwick, Coventry, United Kingdom
[c] Element Six, Global Innovation Centre, Didcot, United Kingdom
[d] Department of Physics, University of Warwick, Coventry, United Kingdom

ARTICLE INFO

Article history:
Received 12 July 2020
Received in revised form
11 September 2020
Accepted 13 September 2020
Available online 18 September 2020

Keywords:
Boron doped diamond
High pressure high temperature synthesis
Porous electrodes
Single particle
Electrochemistry
Scanning electrochemical cell microscopy

ABSTRACT

High pressure high temperature (HPHT) synthesis of crystallographically well-defined boron doped diamond (BDD) microparticles, suitable for electrochemical applications and using the lowest P and T (5.5 GPa and 1200 °C) growth conditions to date, is reported. This is aided through the use of a metal (Fe −Ni) carbide forming catalyst and an aluminum diboride (AlB_2) boron source. The latter also acts as a nitrogen sequester, to reduce boron-nitrogen charge compensation effects. Raman microscopy and electrochemical measurements on individual microparticles reveal they are doped to metal-like levels, contain negligible sp^2 bonded carbon and display a large aqueous solvent window. A HPHT compaction process is used to create macroscopic porous electrodes from the BDD microparticles. Voltammetric analysis of the one-electron reduction of $Ru(NH_3)_6^{3+}$ is used to identify the fundamental electrochemical response of the porous material, revealing large capacitive and resistive components to the current-voltage curves, originating from solution trapped within the pores. Scanning electrochemical cell microscopy is employed to map the local electrochemical activity and porosity at the micron scale. Such electrodes are of interest for applications which require the electrochemical and mechanical robustness properties of BDD, e.g. when operating under high applied potentials/currents, but with the additional benefits of a large, electrochemically accessible, surface area.

1. Introduction

In recent years, boron doped diamond (BDD) has received significant investigation as an electrode material due to its interesting properties compared to traditional metallic and sp^2 bonded carbon electrodes. These include a wide solvent window in aqueous solutions, low background currents, biocompatibility, resistance to fouling and minimal corrosion rates in harsh environments [1–3]. BDD electrodes thus find use in many relevant electrochemical applications including waste-water treatment, electroanalysis, synthesis of both inorganic and organic molecules, and biomolecule sensing [1–3].

To be useful as an electrode material, the boron levels need to be above the metallic doping threshold of ca. 10^{20} B atoms cm^{-3} [3]. This is most easily achieved using chemical vapor deposition (CVD) [4,5], which employs tightly controlled gaseous conditions, resulting in BDD grown in film format on a support material. Compared to high pressure high temperature (HPHT) synthesis [6] which typically employs graphite as the carbon source in conjunction with molten metal catalysts to reduce the growth temperature, CVD growth is a relatively slow and expensive process. In contrast, HPHT synthesis produces large volumes of micron to sub-mm sized, diamond particles often referred to as 'grits', quickly, and at a relatively low cost [7]. HPHT-grown grits have found widespread use in cutting and grinding tools. Diamond grits typically contain a few 100 ppm of nitrogen, incorporated as single substitutional nitrogen impurities (N_s^0) from the atmosphere during growth [8].

* Corresponding author.
E-mail address: j.macpherson@warwick.ac.uk (J.V. Macpherson).

https://doi.org/10.1016/j.carbon.2020.09.038

BDD microparticles are useful cost-effective building blocks for producing hierarchical three dimensional structures for a wide range of electrochemical applications requiring high surface areas, such as gas diffusion electrodes [9], electrical double layer capacitors [10], electrosynthesis [11], electrochemical advanced oxidation [12], electrochemical disinfectant production [13] *etc*. They are also a suitable precursor for processing down to the nanoparticle size [14,15]. However, achieving homogenous boron doping at the levels required for metallic conductivity whilst retaining a well-defined crystallography is challenging in HPHT synthesis. High levels of boron in HPHT diamond causes crystallographic defects [16], which, if significant, will result in an unwanted change in the chemical and physical properties of the BDD particle. Given the presence of nitrogen during HPHT growth, it is also possible for incorporated N_s^0 to electrically compensate boron via electron transfer. Thus, even if the concentration of boron is high, in the presence of nitrogen dopants, N–B charge compensation acts to reduce the concentration of available charge carriers [17]. Thus, measuring the total boron concentration alone, especially with HPHT material, is not sufficient to ascertain viability for electrochemical applications. To reduce nitrogen incorporation into the diamond lattice during HPHT synthesis, nitride forming elements (typically Al, Ti, or Zr) [18] can be added to the solvent/carbon solute matrix.

To date, there has been relatively little research on the HPHT synthesis of BDD particles [16,19–25] Furthermore, of the limited studies undertaken, use of HPHT BDD as an appropriately doped electrochemical material is yet to be demonstrated. In some cases, the boron content is not quantified [16,22], complete experimental conditions are not reported [19,20], or the boron content is insufficient for electrochemical use [21,24]. The highest boron doping levels achieved, $(1.4–2.7) \times 10^{21}$ cm^{-3}, have been obtained using a Mg–Zn (catalyst) B-C system at over 1750 °C (full experimental conditions were not reported) [19]. As Mg and Zn do not form carbides, higher temperature and pressure conditions were required.

By using carbide forming catalyst metals, such as Fe, Ni, Mn, and Co, a reduction in growth temperature and pressure is possible, decreasing the cost and energy required for production [25]. By employing a Co (catalyst) B–C system, HPHT BDD with an estimated boron content of around 10^{20} cm^{-3} was obtained using growth conditions of 8 GPa and 1400–1600 °C. The material was, however, in the form of polycrystalline aggregates in which inhomogeneous boron doping was reported [23]. BDD has also been obtained from a Ni–Mn (catalyst) B–C system, at 5 GPa and 1500–1600 °C, with a boron content of $(2 \pm 1) \times 10^{20}$ cm^{-3} [25]. The particles produced at this doping level were found to have very rough surfaces with a layer-like structure, lacking well-defined crystal faces. For all these studies, no information was provided on the nitrogen levels and no nitrogen sequesters were employed during synthesis.

In this study, we determine HPHT experimental conditions which result in the synthesis of: (i) well-defined (in terms of crystallographic morphology) BDD microparticles, with (ii) sufficiently high, uncompensated, boron levels so that the material is suitable for use as an electrode, and (iii) use of the lowest P and T conditions todate [16,19–25]. We assess the material and electrochemical properties at both the single particle level and in compacted-particle, porous electrode form. To investigate porosity effects in greater detail we employ scanning electrochemical cell microscopy (SECCM) [26]. Here a mobile micro-droplet electrochemical cell is scanned across the surface of the compacted electrode and the voltammetric response used to fingerprint local porosity.

2. Experimental

2.1. Reagents and materials

HPHT BDD material was produced from graphite powder (S9, Morgan Advance Materials), carbonyl iron powder (Fe > 99.5% CIP CN, BASF), carbonyl nickel powder (Ni >99.85%, type 123, Vale), AlB_2 (grade A, H. C. Starck), and US Mesh 100 diamond seed (1.60–1.77 μm diameter, polycrystalline diamond micron grade 2, Element Six Ltd). For particle recovery and cleaning, hydrochloric acid (HCl 37–38%, SG 1.18, Scientific and Chemical Supplies Ltd), nitric acid (HNO_3 68–70%, SG 1.42, Scientific and Chemical Supplies Ltd), sulphuric acid (H_2SO_4 95–97%, SG 1.84, Scientific and Chemical Supplies Ltd), hydrofluoric acid (HF 60%, Euro Lab Supplies Ltd), and potassium nitrate (KNO_3 99.0%, Scientific and Chemical Supplies Ltd) were used. CircuitWorks conductive silver epoxy (Chemtronics) was employed to fix HPHT compacts to Ti/Au coated glass slides for electrochemical characterization.

All solutions were prepared using Milli-Q ultrapure water with a resistivity of 18 MΩ cm (Millipore Corporation). Experiments were carried out at 25 °C unless otherwise stated. For electrochemical characterization, hexaaammineruthenium(III) chloride ($Ru(NH_3)_6Cl_3$ 99%, Strem chemicals) was used as a redox couple and potassium nitrate (KNO_3 99%, Sigma Aldrich) as supporting electrolyte. For electrodeposition of poly(oxyphenylene), phenol (C_6H_5OH >99%, Sigma Aldrich), 2-allylphenol (98%, Sigma Aldrich), 2-*n*-butoxyethanol (99%, Alfa Aesar), ammonium hydroxide (50% v/v aqueous solution, Alfa Aesar), and methanol (MeOH >99.5%, Fisher Scientific) were used.

2.2. HPHT material preparation

10 g of a 'mastermix' was prepared containing 5 g of graphite powder (50 wt%), 3.5 g of iron powder (35 wt%), 1.5 g of nickel powder (15 wt%), and 0.002 g of diamond seed. A single steel ball (10 mm diameter) was added to the mastermix and the pot mixed for 30 min with a turbulent mixer. 1 kg batches of undoped powder were then prepared containing 500 g of graphite (50 wt%), 350 g of iron (35 wt%), 150 g of nickel (15 wt%), and 1.525 g of 'mastermix' (0.305 mg of diamond seed per kg). 200 g of steel balls (10 mm diameter) were added (1:5 mass ratio of steel balls to powder) and mixed for 3 h using a cone blender. This ratio of metal powders was chosen as this is close to the eutectic ratio for a Fe/Ni/C system and thus allows synthesis at the lowest possible P/T conditions, whilst providing a wide P/T operating range. The undoped powder was then mixed with AlB_2, using two different concentrations of AlB_2 expressed as weight % (Table 1). Concentrations of AlB_2 were chosen to ensure an excess of B was available during growth i.e. to produce BDD with $>10^{20}$ B atoms cm^{-3} required for metal-like conductivity.

Steel balls (10 mm diameter, 1:5 ball to powder ratio) were added to these powders which were then mixed for 1 h using a cone blender. The boron containing powder mixtures were sieved to remove the balls, compacted into cylinders (18 g per cylinder) and heated to 1050 °C under vacuum to remove oxygen and hydrogen impurities. Synthesis was then carried out at as low as possible P/T conditions, here ca. 5.5 GPa and 1300 °C in a cubic anvil

Table 1
Composition of boron containing powder mixes.

AlB_2 (wt%)	AlB_2 (g)	Undoped powder mix (g)	Total mass (g)
3.6	19.8	530.2	550
4.8	26.4	523.6	550

HPHT apparatus [27].

To remove residual metals, unreacted graphite and sp^2 bonded carbon formed on the BDD surface, the following cleaning treatment was applied. Specifically, two cylinders were first crushed into small pieces using a Weber press operating at 100 kN. The crushed particles were then heated at 250 °C in HCl (2.0 L) for 22 h. When cool, the solution was decanted through an 80 μm sieve to remove any smaller graphitic residue, and the acid discarded. This process imposes a minimum size of 80 μm in the final particle size distribution. The remaining solids were then subjected to three rinses with deionised water and the BDD particles then boiled at 250 °C in a 3:1 mix of H_2SO_4 and HNO_3 (1.5 L and 0.5 L, respectively) for 22 h. The solution was again decanted through an 80 μm sieve, the acid discarded, and the remaining solids rinsed three times with deionised water. The BDD particles were added to H_2SO_4 (0.5 L) and the solution heated to 300 °C. Once boiling, approximately 10 g of KNO_3 crystals were added and the solution left for an additional 30 min. Once cool, the solution was sieved and washed as previously described. Finally, the BDD particles were added to 100 mL of deionised water in a beaker and placed in an ultrasonic bath (Branson 5510) for 20 min to remove any residual graphite. After this time, the waste water was carefully decanted, and the process repeated until the water remained colorless after ultrasonication. This water was also decanted and the BDD particles left to dry overnight in a 60 °C oven.

To produce HPHT BDD compacted electrodes, herein referred to as "compacts" approximately 2 g of BDD particles were compacted at around 6.6 GPa and 1700 °C in a cubic anvil HPHT apparatus to produce BDD discs. Each compact was treated for 24 h in a mixture of 50 mL HF and 50 mL HNO_3 to release the compacts from the capsule residue. In the absence of metal, at these temperatures, a small degree of BDD to graphite conversion is expected during HPHT compaction. Graphite formation will be prominent in areas where the pressure experienced by the BDD is lower than the nominal applied pressure, due to the microstructure of the compact [28]. A surface de-graphitization treatment was applied by annealing for 5 h at 450 °C in air [29], before polishing one side of each compact to leave a smooth surface, rms roughness ca. 100–200 nm (measured by white light interferometry, Bruker ContourGT). Polishing was achieved using a resin-bonded scaife, embedded with diamond grit particles, whilst rotating and translating the compacts to ensure multidirectional polishing of the surface.

All characterization was carried out on the polished side of the compact, which had a diameter of approximately 16 mm and a thickness of 2 mm. To carry out electrochemical characterization, a titanium (Ti:10 nm)/gold (Au:400 nm) contact was sputtered (Moorfield MiniLab 060 Platform Sputter system) on the unpolished side and annealed in air (400 °C for 5 h) to create an ohmic contact [30]. Each compact was then placed on a Ti/Au coated glass slide with CircuitWorks conductive silver epoxy (Chemtronics) in contact with both the slide and the Ti/Au contact and left to dry in a 60 °C oven for at least 1 h.

Electrodes were also fabricated from single BDD particles (4.8 wt% AlB_2 only). Metal contacts were sputtered onto one end of an individual BDD particle by embedding the particle into silicone WF Gel-Film (Gel-Pak), exposing a single face to the sputter target. Particles were removed from the Gel-Film after sputtering and then annealed as described above. CircuitWorks conductive silver epoxy (Chemtronics) was used to adhere individual particles to lengths of PVC insulated copper wire (RS Components) which had been polished with silicon carbide pads (Buehler) to a point. These were left to dry in an oven (60 °C) for at least 1 h. These assemblies were then sealed using epoxy resin (Epoxy Resin RX771C/NC, Aradur Hardener HY1300GB, Robnor Resins), and dried at room temperature for 72 h. After drying, excess epoxy was removed by carefully polishing with silicon carbide pads (Buehler) of decreasing roughness until the BDD particle was exposed to produce a single particle electrode.

2.3. Material characterization

(i) Raman spectroscopy measurements were performed using a Renishaw inVia Reflex Raman microscope with a 532 nm (2.33 eV) solid state laser, a laser power of 3.6 mW and a Leica N-Plan ×50 objective with an NA of 0.75; giving a spot size of approximately 1 μm. (ii) Field emission scanning electron microscopy (FE-SEM) images of the BDD particles and compacts were taken using the SE2 and InLens secondary electron detectors of a Zeiss Gemini FE-SEM 500 (Zeiss, Germany) operating at 5 kV and 3 kV, respectively. Energy-dispersive X-ray spectroscopy (EDS) measurements of the BDD particles and compacts were recorded using the EDX unit (Oxford Instruments) attached to the microscope, and corresponding images taken using the SE2 detector, at a working distance of 8.5 mm with an accelerating voltage of 20 kV. (iii) Inert gas fusion infrared and thermal conductivity detection (ON736 Oxygen/Nitrogen Elemental Analyzer; LECO Corporation, Michigan, USA) was used to determine the nitrogen content of the particles. (iv) Glow discharge mass spectrometry (GDMS; Evans Analytical Group SAS, Tournefeuille, France) was utilized to characterize the boron content of the HPHT BDD particles. (v) Secondary ion mass spectrometry (SIMS; Loughborough Surface Analysis Limited, Loughborough, UK) was employed to characterize the boron content of the compact disks. (vi) Finally, four point probe measurements were recorded (Jandel RM300) using 100 μm probes arranged in a linear array with 1 mm spacing between probes to determine compact resistivity.

2.4. Electrochemical characterization

Cyclic voltammetry (CV) was carried out using a potentiostat (CHInstruments 600B, 760E, or 800B). A three-electrode droplet cell setup [31] (Fig. S1 in electronic supporting information, ESI 1) was used with the BDD compact as the working electrode, a platinum coil as the counter electrode and a saturated calomel (SCE) (CHI150, IJ Cambria Scientific) or a commercial Ag/AgCl as reference electrodes (DRIREF-2SH, saturated KCl, World Precision Instruments). All potentials are quoted with respect to the reference electrode. All BDD electrodes were oxygen-terminated due to the cleaning procedures adopted prior to use. Each measurement on the compact electrode was recorded for a 1 mm diameter circular area of the surface, achieved by masking with a piece of Kapton tape containing a 1 mm diameter circular hole, cut using a laser (A Series 532 nm Nd:YAG 15 ns pulse green laser, Oxford Lasers Ltd. UK). A droplet of the electrolyte solution (~100 μL) was placed on the electrode surface. The platinum counter electrode was positioned as far away as possible from the electrode surface (ca. 5 mm) in the droplet cell set-up, sufficient to prevent counter electrode electrolysis products interfering with the BDD electrochemical response on the measurement timescale. Before measurements, the surface of each BDD compact was electrochemically cleaned by running CVs between −2.0 V and +0.2 V in 0.1 M H_2SO_4. A standard three-electrode cell set-up was used with the single particle BDD electrodes, with a platinum coil counter electrode and a SCE electrode.

Solvent window and capacitance measurements were run in 0.1 M KNO_3 at a scan rate of 0.1 V s^{-1}. Solvent windows are defined for a geometric current density of ±8.5 mA cm^{-2} for compacts and ±2.0 mA cm^{-2} for single particle electrodes. Limits were chosen where water electrolysis first becomes evident above the background current measured. The electrode response for the fast redox

couple $Ru(NH_3)_6^{3+/2+}$ was also investigated by recording CVs of either 1 mM or 10 mM $Ru(NH_3)_6Cl_3$, in 0.1 M KNO_3 electrolyte, at scan rates in the range 0.005 V s^{-1} to 0.1 V s^{-1}. The BDD compact and BDD single particle electrode, Pt counter electrode, and Ag/AgCl reference electrode were rinsed between different solution measurements.

For SECCM measurements to detect differences in local wetting across the compact electrode, nanopipettes were pulled from borosilicate glass single barrel capillaries (1 mm o.d., 0.5 mm i.d., Harvard Apparatus) using a Sutter P-2000 laser puller (Sutter Instruments, USA). After pulling, the inner diameter of the end of the nanopipettes were ca. 1 μm. The outer walls were silanized by dipping the nanopipette in dichlorodimethylsilane (>99% purity, Acros), while flowing argon through to ensure the inside walls were not silanized. This treatment minimized solution spreading from the pipet onto the sample surface during SECCM measurements (*vide infra*) [32]. The nanopipette was filled with solution containing 10 mM $Ru(NH_3)_6Cl_3$ and 10 mM KNO_3 and an AgCl-coated Ag wire quasi-reference-counter electrode (QRCE) inserted into the back of the nanopipette. A relatively low concentration of supporting electrolyte was used to prevent KNO_3 crystallization during measurements. The experimental setup is shown in ESI 2, Fig. S2. A hopping mode was employed [33], whereby the nanopipette was used to make a series of discrete voltammetric measurements across a 300 × 300 μm area (pixel separation or 'hopping distance' of 5 μm) of the HPHT BDD compact (4.8 wt% AlB_2) surface (working electrode). The uncompensated tip resistance under these conditions was determined to be 15 MΩ from an *I–V* curve measurement [34]. As discussed below, the resulting ohmic drop was relatively small, given the small currents measured. The potential applied to the QRCE was swept from +1 V to −1 V, then back to +1 V at a scan rate of 10 V s^{-1}, and the current at the surface was recorded. All data analysis was performed using Matlab (R2014b, Mathworks).

A high quality CVD grown metal-like doped polycrystalline BDD electrode (350 μm thick, negligible sp^2 bonded carbon content, grown by a commercial microwave CVD process by Element Six Ltd, UK, mechanically polished to sub-nm surface roughness) [35] was used as a control. The crystal orientation of the compact surface for the SECCM scanned area was determined by electron backscatter diffraction (EBSD) using a Zeiss Sigma FE-SEM (Zeiss, Germany) equipped with a Nordlys EBSD detector (Oxford Instruments, UK).

3. Results and discussion

3.1. Material characterization

FE-SEM was employed to investigate the morphology and size of the BDD particles produced via HPHT. To the best of our knowledge, this is the first time crystallographically well-defined HPHT single crystals, which contain BDD at sufficiently high doping levels for electrochemistry, have been observed, as shown in Fig. 1a and b, for 3.6 wt% and 4.8 wt% AlB_2, respectively. The crystals are typically octahedral in shape with the triangular {111} face dominant (Fig. 1a, pink arrow); growth rate of {111} < {100}, as explained by the bald point model (ESI 3, Fig. S3) [16]. From the FE-SEM images recorded ($n = 3$), the growth process resulted in HPHT BDD particles of sizes 80–190 μm (3.6% AlB_2) and 80–180 μm (4.8% AlB_2). 80 μm was a minimum size imposed by the sieving process employed during particle recovery (see HPHT material preparation).

Defects on the surfaces of the crystal faces were observed for both boron concentrations [16], Fig. 1c and d. Similar types and density of defects were observed, regardless of boron concentration, these included small holes and triangular features (green circles), the latter observed predominantly on the {111} face, Fig. 1c. Other more irregularly shaped pits (blue rectangles), Fig. 1c and d, were also noted, although in some locations these could be the result of closely spaced triangular pits. Triangular etch pits are expected on {111} faces [36,37]. Some deformation from perfect crystallinity was observed, particularly evident at the corners of the individual crystals (Fig. 1a and b) along with small crystallite nucleation and growth on the faces of the larger crystals, typically at defect sites (red arrow, Fig. 1d) [38]. EDS measurements indicated that the surfaces of the particles were also free from residual Fe and Ni catalytic metallic impurities (ESI 4, Fig. S4), although it is possible Fe and Ni may still be present in small quantities as internal inclusions buried within the particles. However, these will not affect electrochemical properties as electrochemical processes occur only at the electrode-electrolyte interface.

FE-SEM images were also taken of the polished surface of the BDD microparticle compacted "compact" electrodes (Fig. 2). In polycrystalline CVD grown BDD, differences in SEM contrast between grains has been observed due to varying levels of boron uptake in different crystallographic faces [39]. In Fig. 2 a and b, the black regions represent voids between compressed particles, as no binder is present during compaction to fill these gaps. Metal binders, such as Co and Ni [40], are deliberately excluded here to avoid metallic interferences to the electrochemical response.

Importantly, within and between particles the contrast varies minimally suggesting homogenous boron doping throughout, not unexpected given the prevalence of octahedral {111} faces. Between the large, clearly distinguishable particles are poorly defined areas consisting of much smaller particles. During compaction, some of the larger particles will fracture and fill appropriately sized gaps between particles. A greater extent of connection, with fewer and smaller holes between particles was observed for the 4.8 wt% AlB_2 additive (Fig. 2a) compared to 3.6 wt% AlB_2 (Fig. 2b) where BDD particles appear more isolated and distinct. Tentatively this could suggest that the higher doped BDD particles fracture more easily under the high pressures applied, producing the smaller fragments/particles required to fill the gaps.

To provide information on boron doping levels, Raman spectra were taken of the two differently boron doped compacts (Fig. 3) and compared to the spectrum obtained for an HPHT single diamond crystal (contains nitrogen at doping levels typically 200–300 ppm [41]; ca. 3–6 × 10^{19} N atoms cm^{-3}). The presence of boron in the diamond lattice is confirmed by peaks at ~550 cm^{-1} and ~1200 cm^{-1}, a signature of highly doped BDD and not observed in the diamond crystal [42]. The 550 cm^{-1} peak has been attributed to the local vibration modes of boron pairs within the lattice [43]. The broad 1200 cm^{-1} band corresponds to a maximum in the phonon density of states which arises from the disorder introduced by boron doping [44].

The BDD Raman line is also red-shifted slightly relative to the diamond line (1332.5 cm^{-1}; Fig. 3a), occurring at 1330.83 cm^{-1} and 1329.15 cm^{-1} for 3.6 wt% AlB_2 and 4.8 wt% AlB_2, respectively. This shift is due to boron impurity scattering which causes a tensile residual stress [45]. The larger magnitude shift is observed for the 4.8 wt% AlB_2 compact, indicating a higher boron doping level than for the 3.6 wt% AlB_2 compact, as expected. A slight asymmetry of this peak is also observed due to a Fano resonance [46], indicative of metal-like conductivity [47]. No graphite peaks are present (the *G* and *D* peaks lie at ca. 1560 cm^{-1} and 1360 cm^{-1} respectively) [48] indicating removal of any sp^2 bonded carbon impurities introduced either during growth or the compaction process, within the resolution of the measurement. Raman spectra for the individual HPHT BDD particles were also obtained (ESI 5, Fig. S5) and the same key features observed. As the Raman spot size (ca. 1 μm) was significantly smaller than the size of a particle, spectra can be recorded on individual particles. No significant difference was seen between particles. This again is supportive of the observation that the vast

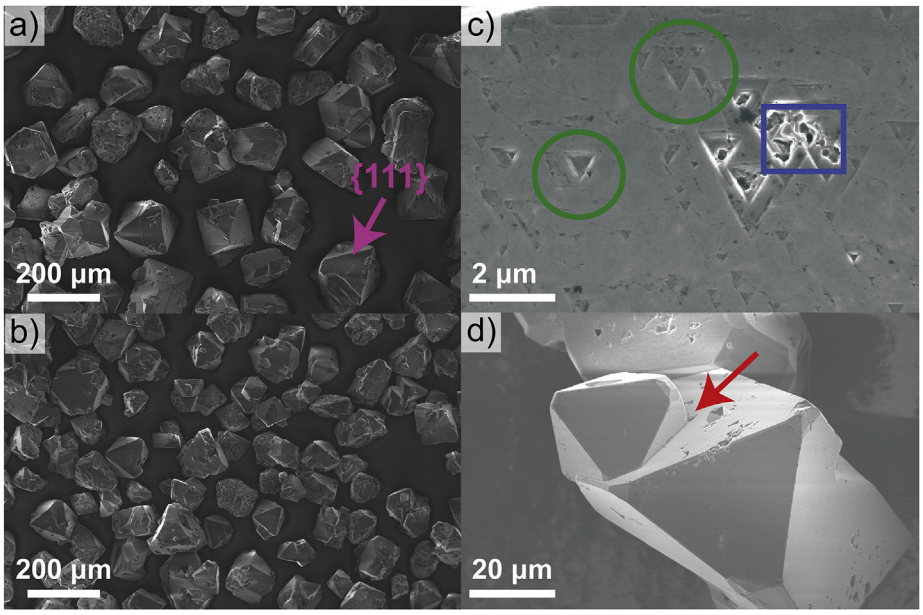

Fig. 1. FE-SEM images showing morphology (a and b), and surface defects (c, close up of {111} face, and (d) of HPHT BDD particles made with 3.6 wt% AlB_2 (a and c) and 4.8 wt% AlB_2 (b and d). Red arrows indicate surface nucleation and green circles and blue rectangles indicate triangular pits and irregularly shaped holes, respectively. (A colour version of this figure can be viewed online.)

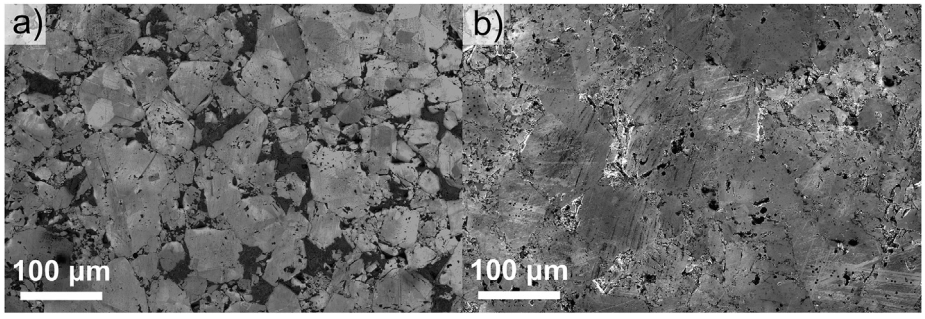

Fig. 2. FE-SEM images showing surface structure of the polished compact electrodes produced from HPHT BDD particles synthesized using 3.6 wt% AlB_2 (a) and 4.8 wt% AlB_2 (b).

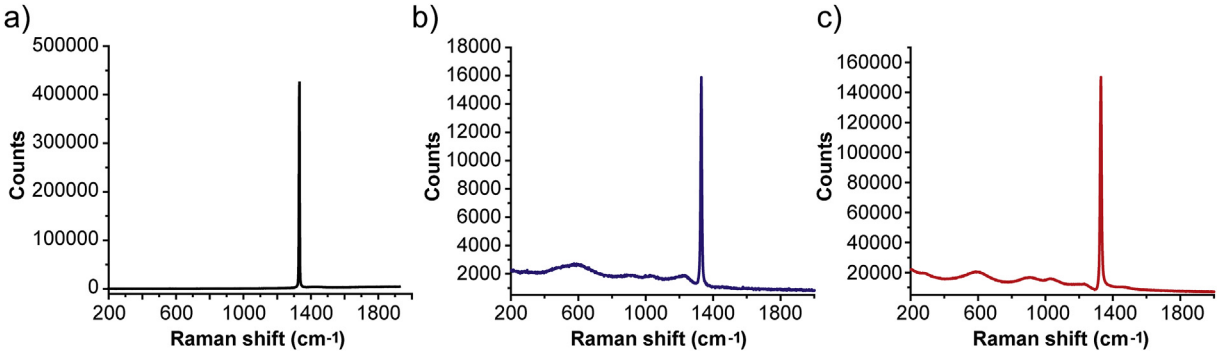

Fig. 3. Raman spectra of (a) HPHT diamond, and HPHT BDD compacts at (b) 3.6 wt% and (c) 4.8 wt% AlB_2 additive. BDD peaks observed at 550 cm^{-1} and 1200 cm^{-1}, along with an asymmetry due to Fano resonance and redshift in the intrinsic diamond peak at 1330.83 cm^{-1} (3.6 wt% AlB_2) and at 1329.15 cm^{-1} (4.8 wt% AlB_2). (A colour version of this figure can be viewed online.)

majority of particles grown are of the same crystallographic orientation.

SIMS and GDMS analysis of the two differently boron doped compacts are given in Table 2 and provide information on the total boron and nitrogen dopant levels. Both compacts are above 10^{20} B atoms cm^{-3} [3], with higher [B_{total}] for the larger wt% of AlB_2 added. With no concern for nitrogen doping these would be indicative of suitable boron dopant levels for metal-like conductivity. However, in HPHT growth nitrogen doping must also be considered. The measured nitrogen content was found to be more than one order of

Table 2
[B_{total}] from glow discharge and secondary ion mass spectrometry (GDMS and SIMS, respectively), [N_{total}] from LECO nitrogen elemental analysis.

AlB_2 (wt%)	[B_{total}] from GDMS (atoms cm^{-3})	[B_{total}] from SIMS (atoms cm^{-3})	[N_{total}] (atoms cm^{-3})
3.6	$2.0 \pm 0.4 \times 10^{20}$	$1.3 \pm 0.1 \times 10^{20}$	$7.7 \pm 0.4 \times 10^{18}$
4.8	$2.9 \pm 0.6 \times 10^{20}$	$1.9 \pm 0.1 \times 10^{20}$	$4.2 \pm 0.1 \times 10^{18}$

magnitude lower than the boron content (Table 2). The data indicates nitrogen compensation effects will not be significant, also concluded from the Raman data in Fig. 3, which show BDD peaks with accompanying Fano resonances.

3.2. Electrochemical characterization

3.2.1. Macroscopic measurements

Electrochemical characterization of the polished surface of the two differently doped BDD compacts was performed. Data for the 3.6 wt% AlB_2 compact are shown in blue, and data for the 4.8 wt% AlB_2 compact are shown in red, Fig. 4. The solvent windows, for each material (Fig. 4a) in 0.1 M KNO_3 at 0.1 V s^{-1}, were wide and featureless, with values of 2.64 V and 2.95 V for 3.6 wt% AlB_2 and 4.8 wt% AlB_2 (for a given geometric current density of $\pm$8.5 mA cm^{-2}) respectively. To calculate the electrochemical capacitance, *C*, the voltage window was decreased to 0 V $\pm$ 0.1 V (Fig. 4b) and equation (1) was used:

$$C = \frac{i_{av}}{\nu A} \quad (1)$$

where i_{av} is the average current magnitude at 0 V from the forward and reverse sweep, ν is the scan rate (0.1 V s^{-1}) and *A* is the geometric electrode area. The sloping response of the CV in Fig. 4b indicates both a significant resistive contribution, as well as a capacitive component.

For polished CVD-grown BDD a *C* of $\leq$10 μF cm^{-2} is typical [35]. The *C* values for the compact electrode are almost three orders of magnitude larger, 3.1 mF cm^{-2} for 3.6 wt% AlB_2 and 2.6 mF cm^{-2} for 4.8 wt% AlB_2. However, as the CV is sloped rather than rectangular in shape, due to resistive contributions, these values should be considered as approximates. This is also true of the solvent window values, where ohmic drop contributions are also likely to be present. In accordance with the FE-SEM images in Fig. 2, this suggests that there is an almost three orders of magnitude larger electrochemically accessible surface area, due to the porosity of the compact. The porosity results from the voids present between particles, as seen in Fig. 2. There is also the possibility of porosity

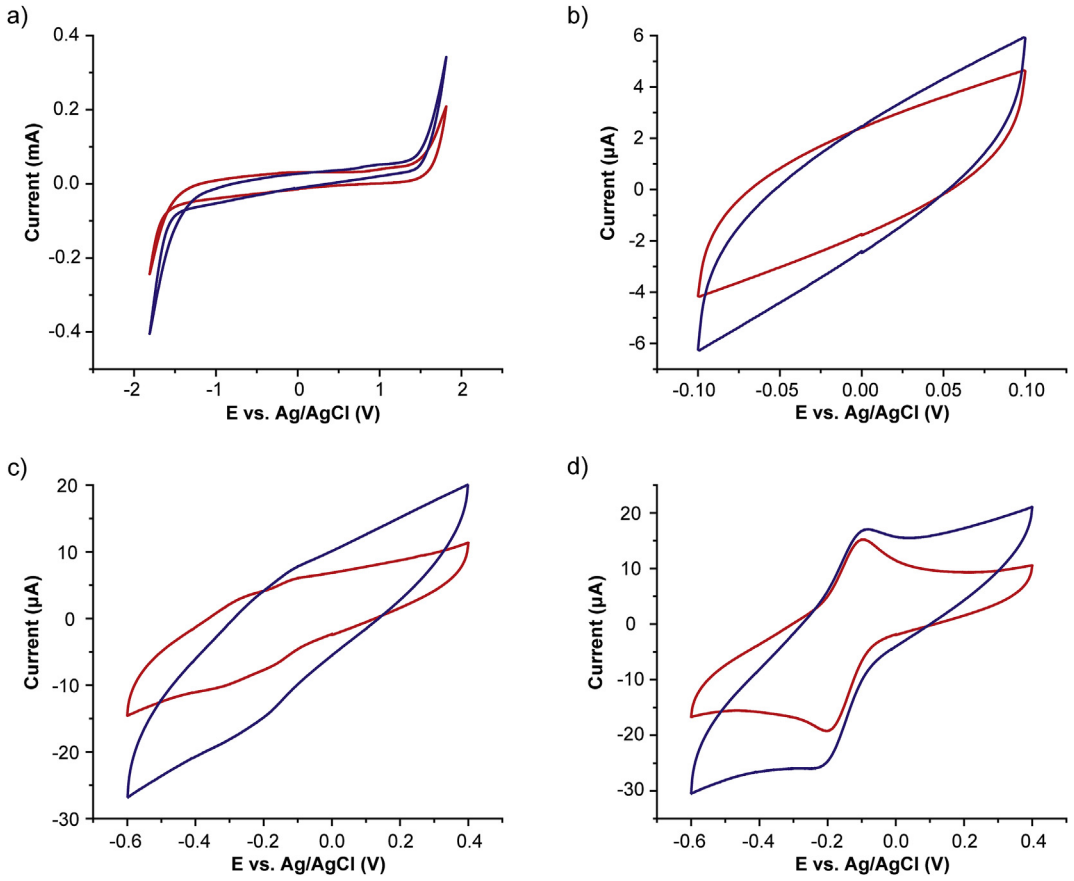

Fig. 4. CVs recorded in 0.1 M KNO_3 at a scan rate of 0.1 V s^{-1} at the polished HPHT BDD compacts with 3.6 wt% AlB_2 (blue) and 4.8 wt% AlB_2 (red). Shown are (a) solvent windows, (b) typical capacitance curves recorded to calculate capacitance, and electrode response in (c) 1 mM and (d) 10 mM $Ru(NH_3)_6^{3+/2+}$. (A colour version of this figure can be viewed online.)

arising from sub-micron sized fractures, present within the particles and introduced during the compaction process. For some electrochemical applications, *e.g.* electrochemical supercapacitors, high capacitance materials are desired [49,50]; although not the focus here this will be explored in the future.

For the two different compact electrodes, from four-point probe resistivity measurements (in air), taking into account electrode geometry, resistance values of 0.48 ± 0.06 Ω and 0.27 ± 0.03 Ω for 3.6 wt% AlB_2 and 4.8 wt% AlB_2, respectively, were determined; see ESI 6 for further details. These values demonstrate that the compaction process is successful at producing a low-resistance, well-connected BDD particle to BDD particle, HPHT electrode. The ohmic drop (iR) contribution, assuming just these resistance values, will be negligible when considering the currents passed in Fig. 4c and d. However, the CVs in Fig. 4b, show non-zero, approximately linear gradient backgrounds, suggesting a significantly higher resistance when the electrodes are immersed in the electrolyte solution: 15.4 ± 9.5 kΩ and 10.0 ± 5.4 kΩ for 3.6 wt% AlB_2 and 4.8 wt % AlB_2 compact electrodes, respectively (taking the voltage range 0.0−0.1 V and simply applying Ohm's law). We attribute this resistance to solution porosity; solution trapped within the small pores results in significant, high solution resistance, manifested in the electrochemical measurement.

To provide information on the electrochemical performance properties of the material, the one-electron reduction of $Ru(NH_3)_6^{3+}$ was studied by CV. Due to the large background currents, the reduction and oxidation peaks for CV of 1 mM $Ru(NH_3)_6^{3+}$ are difficult to discern (Fig. 4c) over the background at this scan rate (0.1 V s^{-1}). Note that for an identical cell set-up and CV scan conditions on planar CVD-grown BDD, the $Ru(NH_3)_6^{3+}$ response is close to reversible (diffusion-controlled), with a 62 mV peak to peak separation, ΔE_p (ESI 7, Fig. S7). Increasing the concentration of $Ru(NH_3)_6^{3+}$ to 10 mM (Fig. 4d), improves the CV response of the compact electrodes, with ΔE_p values of 125 mV and 104 mV for 3.6 wt% AlB_2 and 4.8 wt% AlB_2, respectively. The larger ΔE_p values, compared to the response of the CVD BDD electrode in 1 mM $Ru(NH_3)_6^{3+}$ (ESI 7, Fig. S7), again indicate uncompensated resistance (ohmic drop). However, the apparent uncompensated resistances in these CVs are significantly less than would be deduced from the resistance values derived from the capacitive curves in Fig. 4b. This is because as the pore solution resistance increases with increasing solution penetration depth there will be a concomitant decrease in the driving force for the redox process. This results in a natural depth limit at which the redox reaction can no longer occur for a given applied potential range. A major component to the redox process is thus from the top surface of the electrode (planar diffusion), exposed directly to the solution, where ohmic drop contributions are less significant.

3.2.2. Local electrochemical measurements

To further understand porosity and pore solution resistance contributions to the electrochemical response of the compact electrodes, SECCM measurements were performed using a 1 μm-diameter pipette. This pipette was sufficiently small such that it was possible to make measurements on individual crystal faces of the compact. CVs were recorded in 10 mM $Ru(NH_3)_6^{3+}$ and 10 mM KNO_3. A typical voltammetric response, on a (111) facet of a 4.8 wt% AlB_2 HPHT compact, identified using EBSD analysis (*vide infra*), is shown in Fig. 5a. This response is compared to a typical CV obtained under the same conditions but using a CVD-grown polished polycrystalline BDD electrode, Fig. 5b. Detailed analysis of all CVs on the 4.8 wt% AlB_2 HPHT BDD compact is provided in Fig. 6 (*vide infra*).

In all cases, the SECCM tip was landed at a working electrode potential of 1 V vs QRCE. Immediately upon meniscus contact with the substrate (but no contact of the pipette), the voltammetric scan commenced, at a fast rate of 10 V s^{-1} to prevent significant wetting on the timescale of the scan, given the hydrophilic nature of oxygen terminated BDD [32]. For the compact, at the start of the scan (1 V vs QRCE), the current is close to zero, but as the potential is scanned cathodically, a reduction current begins to flow at approximately −0.3 V and increases monotonically as the potential is scanned further in the negative direction. At −1.0 V vs QRCE, the scan direction is reversed and the current decreases in magnitude towards 0 nA, before an anodic peak is observed in the potential range −0.2 V to +0.5 V. Notably, the reduction current magnitudes for the HPHT electrode (Fig. 5a) are much higher when compared to the CVD sample (Fig. 5b). A different CV shape is also observed; the reduction peak of $Ru(NH_3)_6^{3+}$ at −0.75 V is pronounced for the CVD electrode but not observed for the HPHT electrode. An estimation of the electron transfer kinetic rate constant for CVD grown BDD was obtained from Fig. 5b using DigiElch software [51] (= 5×10^{-3} cm s^{-1}), for details see ESI 8, which is broadly in line with previous values [35].

The larger current magnitudes in the reduction sweep are indicative of porosity effects. During the $Ru(NH_3)_6^{3+}$ reduction process (O to R in Fig. 5), there is solution ingress into the body of the electrode, as shown schematically in Fig. 5a. This results in high mass transport as a result of solution flow into the electrode and a larger accessible electrode area, compared to the corresponding planar surface. The current magnitude increases during the forward (cathodic) scan, but for this measurement location, does not peak. This indicates that, overall, there is insufficient driving force for transport-controlled electrolysis of $Ru(NH)_6^{3+}$ at some parts of the electrode (deep within the pores) due to the high solution resistance.

As the potential scan direction is reversed in the anodic direction, solution will continue to flow into the porous BDD, carrying the product, $Ru(NH)_6^{2+}$ (O in Fig. 5a), which is re-oxidized on the return sweep. The peak current for the compact electrode is smaller and much broader than that for the planar surface (Fig. 5b), indicating re-oxidation occurs mainly within the resistive body of the electrode. As the scan area for each CV is typically much smaller than the average particle size, these data provide further evidence that the individual crystal faces are also porous, likely due to sub-micron sized fractures created during compaction, in addition to voids present between particles, Fig. 2.

Porosity of the intrinsic material was also confirmed by electrochemically coating the HPHT BDD compact with an insulating layer of poly(oxyphenylene) [52] and observing the electrochemical response (ESI 9, Figs. S8 and S9). As the coating method is electrochemical, all accessible wetted areas of the electrode should be available for insulation by the polymerized insulating material. This was confirmed by the absence of an electrochemical response when coated. Gentle polishing was employed to remove the insulating polymer, predominantly from the top surface of the compact, but leaving all accessible sub-surface pores and voids, between and within particles, filled. Under these conditions, a clearer CV emerges, with much smaller current magnitude and significantly reduced capacitive contributions (ESI 9, Fig. S9) compared to the CV recorded on the bare compact.

A key aspect of SECCM for polycrystalline electrode materials is that the spatial distribution of electrochemical processes can be investigated as a function of surface structure [53]. EBSD demonstrates that the surface of a compact electrode now comprises different crystallographic regions (Fig. 6a). Whilst the compact is predominantly formed using octahedral {111} crystals, polishing of the compact surface results in different regions being exposed. Most are due to well-defined low index crystal planes, although there are areas where the plane orientations are less well-defined on the spatial resolution of EBSD. These areas contain much

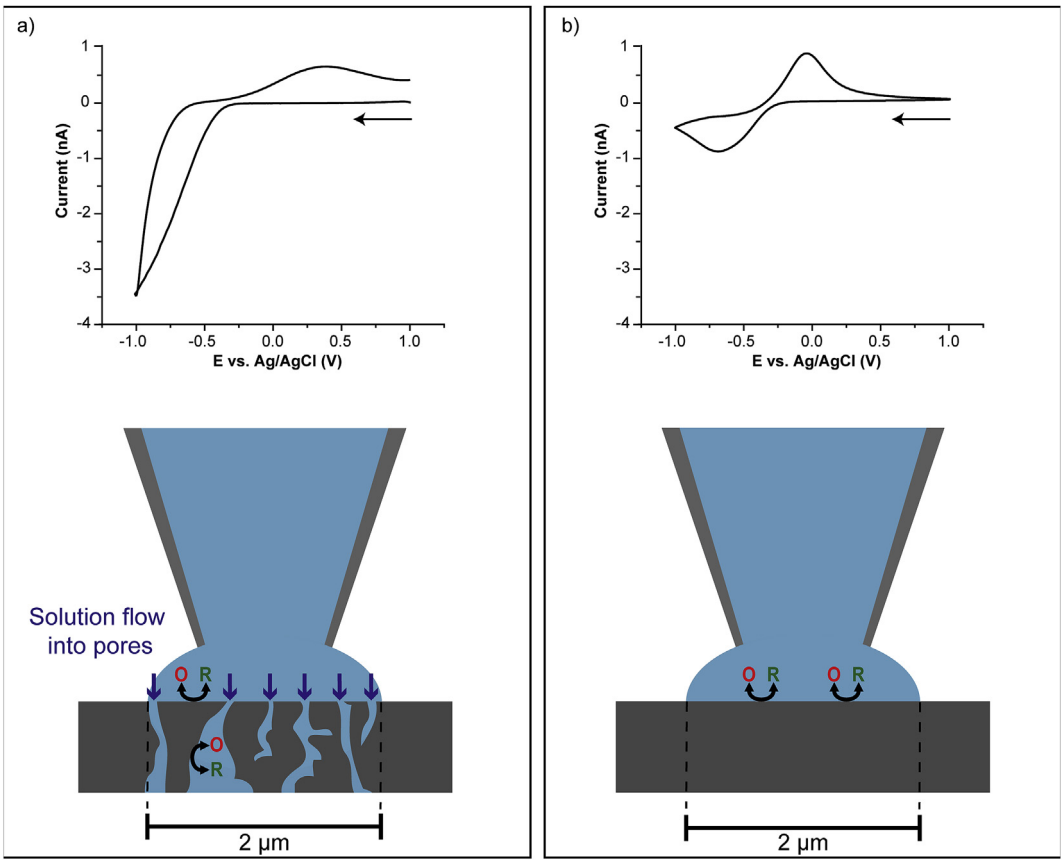

Fig. 5. Typical CVs recorded in 10 mM $Ru(NH_3)_6Cl_3$ and 10 mM KNO_3 at 10 V s^{-1} with a 1 μm sized nanopipette on (a) a (111) facet of the 4.8 wt% AlB_2 HPHT BDD compact and (b) a high quality CVD grown BDD sample with schematics to show how electron transfer is occurring at each electrode surface. (A colour version of this figure can be viewed online.)

smaller BDD particles, created during HPHT grit compaction, and voids, both previously observed in the FE-SEM images in Fig. 2.

A map of onset cathodic potential as a function of tip position, defined as the potential where the current was twice the standard deviation of the background current (= −0.24 nA) is shown in Fig. 6b. The map does not reveal any correlation of onset potential with crystallographic orientation (Fig. 6a). This is not unexpected given that the boron dopant density is likely to be fairly uniform across the surface as the compact is formed mainly from {111} crystals. Voltammetric responses from four marked locations in Fig. 6b are shown in Fig. 6c. They are typical of those obtained at different locations across the surface. The full dataset of CVs recorded is provided along with a MATLAB data reading script which can be downloaded with the ESI and allows the reader to visualize the CV response for each pixel ($n = 400$) in Fig. 6b (see ESI 10 for full instructions).

Response 3 most closely resembles that shown in Fig. 5a. For those curves which show higher cathodic activity on the forward reduction sweep (1 and 2), there is a limiting cathodic current and higher anodic activity on the reverse sweep. Moreover, the larger the forward cathodic current magnitude, the more negative the potential of the anodic peak. A detailed analysis of all 400 CVs in Fig. 6d further highlights this correlation by plotting the onset potentials for the cathodic and anodic sweep of each curve (defined as −0.24 nA on the cathodic and +0.24 nA on the anodic). A linear line slope ca. 2.5 results, i.e. the less cathodic the process the less anodic the reverse process (smaller separation), and the more facile (less resistive) the electrochemical response. Facile electrochemistry is attributed to solution ingress into less resistive, more open, internal structures, which in turn give rise to larger current magnitudes and a transport-limited steady-state response on the cathodic scan.

Local capacitance values were estimated from equation (1), at 0.95 V, free from faradaic contributions, from the forward sweep only, measured immediately upon contacting the electrode surface with the nanopipette. The exposed geometric electrode area, A, during individual measurements was estimated to be 6.8 ± 2.0 μm^2, calculated from meniscus residues observed in FE-SEM secondary electron images ($n = 24$, ESI 11, Fig. S11b). Extracted capacitance values were 12 ± 3.6 μF cm^{-2}, two orders of magnitude lower than the macroscopic measurements previously detailed, and close to those recorded for a planar CVD BDD electrode (≤10 μF cm^{-2}) [35]. When measuring the capacitance after a 1 s contact, compared with that measured upon immediate contact of droplet to electrode, the mean value increased approximately fourfold to 56 ± 17 μF cm^{-2} (ESI 12, Fig. S12). This again supports the idea of significant substrate porosity: on a relatively short time scale solution leaks into pores, the accessible electrode area increases, and so does the local capacitance.

3.3. Electrochemical characterization of individual BDD particles

The electrochemical behavior of a single BDD particle was also investigated. Studies were performed on single BDD particles (grown using 4.8 wt% AlB_2) sealed in insulating epoxy resin with a {111} surface exposed through gentle abrasion. Fig. 7 shows an FE-SEM image of the top surface ({111} face) of an alumina polished single particle electrode, Fig. 8a. The electrode is irregularly shaped,

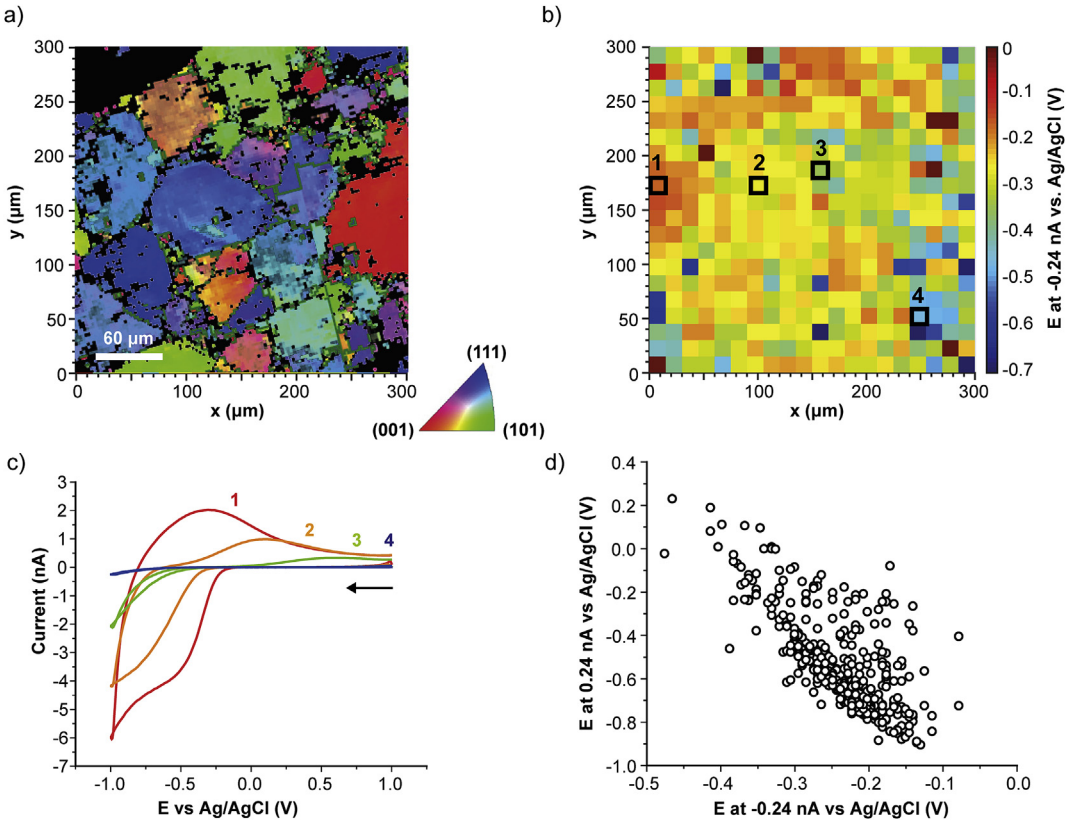

Fig. 6. (a) EBSD image and (b) map of onset potentials of the SECCM scan area on the 4.8 wt% AlB_2 HPHT BDD compact. Onset potential was defined as the potential (E) at −0.24 nA on the cathodic sweep. Black squares in (b) indicate the locations where the CVs shown in (c) were recorded. The CVs for each pixel in the image are provided in ESI 10. All CVs were recorded in 10 mM $Ru(NH_3)_6Cl_3$ and 10 mM KNO_3 at 10 V s^{-1}. Arrow indicates initial scan direction. (d) Correlation between the potential at −0.24 nA on the cathodic sweep and the potential at +0.24 nA on the anodic sweep of all recorded CVs. (A colour version of this figure can be viewed online.)

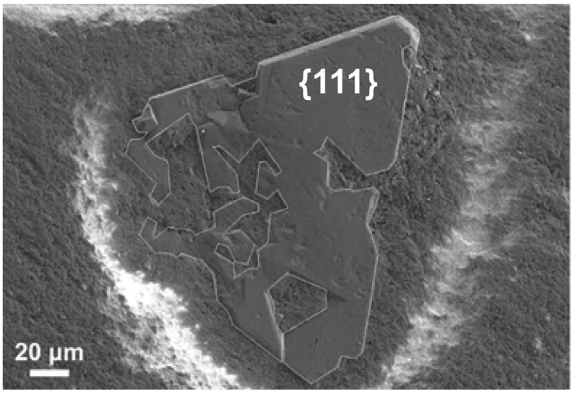

Fig. 7. FE-SEM image showing an HPHT BDD particle of a single particle electrode embedded in insulating epoxy resin. The white outline illustrates exposed alumina polished as-grown BDD.

ca. 1.3×10^{-4} cm^2 in geometric area, determined using ImageJ [54].

For this electrode, the solvent window of 2.93 V (defined by a geometric current density of ±2.0 mA cm^{-2}), at 0.1 V s^{-1}, in aerated 0.1 M KNO_3, is flat and featureless (Fig. 8b). From the CV scan (Fig. 8c), a capacitance value of 46 μF cm^{-2} is determined, using equation (1). This is likely to be an overestimation as FE-SEM shows the BDD surface is not featureless and thus the geometric area underestimates the electrochemically accessible area. No electrochemical features associated with sp^2 bonded carbon are present [35]. Fig. 8d shows the CV response for 1 mM $Ru(NH_3)_6^{3+/2+}$ over the scan range 0.005 V s^{-1} to 0.1 V s^{-1}.

As the scan rate is decreased, the CV changes morphology from peak-shaped to almost sigmoidal in response, as expected for a microelectrode of this size: at the higher scan rates linear diffusion dominates, whilst an increasing radial contribution prevails at slower scan rates [55]. From the limiting current, $i_{lim} = 23.7$ nA, an approximate value for the electrode radius, a, (assuming a disk geometry and a diffusion coefficient, D, value for $Ru(NH_3)_6^{3+}$ of 8.8×10^{-6} cm^2 s^{-1}) [56] is 69.8 μm, calculated using equation (2):

$$i_{lim} = 4naFDc^* \quad (2)$$

where F is the Faraday constant, n (=1) is the number of electrons transferred, and c^* is the bulk concentration of $Ru(NH_3)_6^{3+}$ [55,57]. When the Tomeš criterion of reversibility - which states that for a reversible charge transfer process the difference in quartile potentials, $|E_{1/4}\text{-}E_{3/4}|$, equals 59 mV for a one electron transfer process at 298 K - is applied to the CV recorded at the slowest scan rate of 0.005 V s^{-1} (Fig. 8d red line), a value for $|E_{1/4}\text{-}E_{3/4}|$ of 54 mV is obtained [55,58]. Note that $|E_{1/4}\text{-}E_{3/4}|$ is slightly below the Tomes criterion for reversibility because although the CV reaches a plateau, the mass transport rate is insufficiently high for the process to be at true steady-state during the course of the scan. For nominally steady-state techniques, the effect is to make the voltammogram steeper (i.e. smaller $|E_{1/4}\text{-}E_{3/4}|$) as seen here [59]. This result provides further compelling evidence that these particles are doped sufficiently to be considered metal-like for electrochemical applications and contain negligible sp^2 bonded carbon.

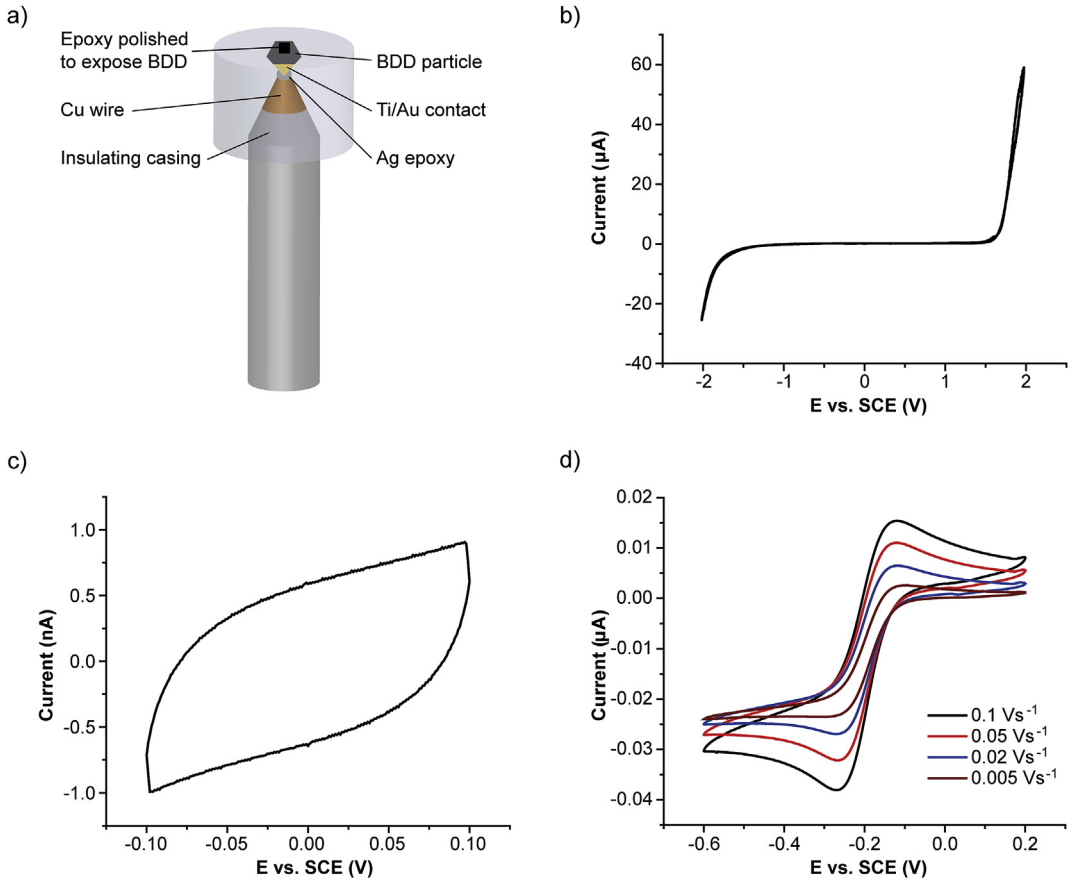

Fig. 8. (a) Schematic to show the structure of the HPHT BDD SPE. CVs recorded in 0.1 M KNO_3 at a scan rate of 0.1 V s^{-1} at the HPHT BDD SPE (4.8 wt% AlB_2 additive showing (b) the solvent window, (c) a typical capacitance curve and (d) the electrode response in 1 mM $Ru(NH_3)_6^{3+/2+}$ and 0.1 M KNO_3 at scan rates of 0.1, 0.05, 0.02, and 0.005 V s^{-1}. (A colour version of this figure can be viewed online.)

4. Conclusion

Well-defined crystallographic (octahedral with {111} faces dominant) BDD microparticles (<200 μm in size) containing negligible sp^2 bonded carbon and suitable for electrochemical applications, were synthesized using HPHT. Boron doping levels were above those required for metal-like conductivity. Synthesis of these particles represent an exciting step forward in the large scale, cost-effective production of electrochemically-viable BDD particles. Such materials can function as building blocks for both the bottom-up production of cheaper high surface area BDD-based electrodes and the top-down production of smaller BDD nanoparticles. The use of a Fe–Ni carbide forming catalyst aided in enabling lower temperatures and pressures than previously reported, ~5.5 GPa and 1200 °C, whilst AlB_2 functioned as both a source of B and nitrogen sequester.

HPHT compaction was shown to be an effective method for creating macroscopic high surface area, low material resistance, porous electrode structures from the BDD particles. The porosity originates from voids between particles and likely sub-micron fractures with particles, formed during material compaction. CV analysis proved useful at assessing the impact of electrode porosity at the macro-level, showing a three orders of magnitude increase in double layer capacitance compared to a planar non-porous CVD-grown electrode. Changing the compaction conditions will be one way to manipulate electrode porosity in the future. We envisage these HPHT BDD electrodes will be of great interest for applications where high surface area and porosity are useful attributes, with the added benefits of corrosion stability and a large aqueous solvent window e.g. gas porous electrodes, electrocatalyst or enzyme support structures, electrochemical supercapacitors, electrosynthesis, electrochemical advanced oxidation, electrochemical disinfectant production. It may even be possible to determine compaction conditions where the BDD porosity is negligible. The resulting electrode material would then become attractive for electroanalysis and electron transfer kinetic studies.

SECCM was employed as a new method to detect and fingerprint electrode porosity at the micro-level. For porosity mapping, the voltammetric waveshape was shown to be diagnostic of the ingress of electrolyte solution into the porous electrode and a qualitative mark of the local pore dimensions. There are further ways in which SECCM could be developed for porosity mapping in the future, including measuring capacitance alongside the redox process to reveal the internal electrode surface area, which would allow more detailed analysis of the redox process. The use of different voltammetric scan rates or chronoamperometry could also be beneficial in quantifying porosity as a function of solution ingress.

CRediT authorship contribution statement

Georgia F. Wood: Methodology, Validation, Formal analysis, Investigation, Writing - original draft, Visualization. **Carmen E. Zvoriste-Walters:** Conceptualization, Methodology, Formal analysis. **Mark G. Munday:** Conceptualization, Methodology, Formal analysis. **Mark E. Newton:** Writing - review & editing. **Viacheslav Shkirskiy:** Methodology, Formal analysis, Writing - original draft.

Patrick R. Unwin: Formal analysis, Writing - review & editing, Supervision. **Julie V. Macpherson:** Conceptualization, Writing - original draft, Visualization, Supervision, Project administration, Funding acquisition.

Declaration of competing interest

The authors declare that they have no known competing financial interests or personal relationships that could have appeared to influence the work reported in this paper.

Acknowledgements

The authors would like to acknowledge the Warwick Electron Microscopy Research Technology Platform and the WMG Advanced Manufacturing and Materials Centre at the University of Warwick for the use of their electron microscopes. GW was funded by the EPSRC Centre for Doctoral Training in Diamond Science and Technology (EP/L015315/1). The authors acknowledge Dr. Haytham Hussein for assistance with SEM and Dr. Gabriel Meloni for assistance with EDS measurements (Warwick Chemistry). VS acknowledges financial support from the European Union's Horizon 2020 research and innovation programme under grant agreement 792948 (NELMA). PRU thanks the Royal Society for a Wolfson Research Merit Award.

Appendix A. Supplementary data

Supplementary data to this article can be found online at https://doi.org/10.1016/j.carbon.2020.09.038.

References

[1] N. Yang, S. Yu, J.V. MacPherson, Y. Einaga, H. Zhao, G. Zhao, G.M. Swain, X. Jiang, Conductive diamond: synthesis, properties, and electrochemical applications, Chem. Soc. Rev. 48 (2019) 157–204, https://doi.org/10.1039/c7cs00757d.

[2] S.J. Cobb, Z.J. Ayres, J.V. Macpherson, Boron doped diamond: a designer electrode material for the twenty-first century, Annu. Rev. Anal. Chem. 11 (2018) 463–484, https://doi.org/10.1146/annurev-anchem-061417-010107.

[3] J.V. Macpherson, A practical guide to using boron doped diamond in electrochemical research, Phys. Chem. Chem. Phys. 17 (2015) 2935–2949, https://doi.org/10.1039/c4cp04022h.

[4] J.C. Angus, H.A. Will, W.S. Stanko, Growth of diamond seed crystals by vapor deposition, J. Appl. Phys. 39 (1968) 2915–2922, https://doi.org/10.1063/1.1656693.

[5] P.W. May, Y.A. Mankelevich, From ultrananocrystalline diamond to single crystal diamond growth in hot filament and microwave plasma-enhanced CVD reactors: a unified model for growth rates and grain sizes, J. Phys. Chem. C 112 (2008) 12432–12441, https://doi.org/10.1021/jp803735a.

[6] H.P. Bovenkerk, F.P. Bundy, H.T. Hall, H.M. Strong, R.H. Wentorf, Preparation of diamond, Nature 184 (1959) 1094–1098, https://doi.org/10.1038/1841094a0.

[7] M.A. Prelas, G. Popovici, L.K. Bigelow, Handbook of Industrial Diamonds and Diamond Films, Marcel Dekker, 1998. https://books.google.co.uk/books/about/Handbook_of_Industrial_Diamonds_and_Diam.html?id=X3qe9jzYUAQC&redir_esc=y. (Accessed 25 July 2017).

[8] I. Kiflawi, H. Kanda, S.C. Lawson, The effect of the growth rate on the concentration of nitrogen and transition metal impurities in HPHT synthetic diamonds, Diam. Relat. Mater. 11 (2002) 204–211, https://doi.org/10.1016/S0925-9635(01)00569-6.

[9] Y.G. Wang, L. Cheng, F. Li, H.M. Xiong, Y.Y. Xia, High electrocatalytic performance of Mn3O4/mesoporous carbon composite for oxygen reduction in alkaline solutions, Chem. Mater. 19 (2007) 2095–2101, https://doi.org/10.1021/cm062685t.

[10] O. Barbieri, M. Hahn, A. Herzog, R. Kötz, Capacitance limits of high surface area activated carbons for double layer capacitors, Carbon N. Y. 43 (2005) 1303–1310, https://doi.org/10.1016/j.carbon.2005.01.001.

[11] T.A. Ivandini, Y. Einaga, Polycrystalline boron-doped diamond electrodes for electrocatalytic and electrosynthetic applications, Chem. Commun. 53 (2017) 1338–1347, https://doi.org/10.1039/c6cc08681k.

[12] F.C. Moreira, R.A.R. Boaventura, E. Brillas, V.J.P. Vilar, Electrochemical advanced oxidation processes: a review on their application to synthetic and real wastewaters, Appl. Catal. B Environ. 202 (2017) 217–261, https://doi.org/10.1016/j.apcatb.2016.08.037.

[13] Y. Honda, T.A. Ivandini, T. Watanabe, K. Murata, Y. Einaga, An electrolyte-free system for ozone generation using heavily boron-doped diamond electrodes, Diam. Relat. Mater. 40 (2013) 7–11, https://doi.org/10.1016/j.diamond.2013.09.001.

[14] S. Heyer, W. Janssen, S. Turner, Y.G. Lu, W.S. Yeap, J. Verbeeck, K. Haenen, A. Krueger, Toward deep blue nano hope diamonds: heavily boron-doped diamond nanoparticles, ACS Nano 8 (2014) 5757–5764, https://doi.org/10.1021/nn500573x.

[15] S. Nantaphol, R.B. Channon, T. Kondo, W. Siangproh, O. Chailapakul, C.S. Henry, Boron doped diamond paste electrodes for microfluidic paper-based analytical devices, Anal. Chem. 89 (2017) 4100–4107, https://doi.org/10.1021/acs.analchem.6b05042.

[16] J.Q. Zhang, H.A. Ma, Y.P. Jiang, Z.Z. Liang, Y. Tian, X. Jia, Effects of the additive boron on diamond crystals synthesized in the system of Fe-based alloy and carbon at HPHT, Diam. Relat. Mater. 16 (2007) 283–287, https://doi.org/10.1016/j.diamond.2006.06.005.

[17] R.M. Chrenko, Boron, the dominant acceptor in semiconducting diamond, Phys. Rev. B 7 (1973) 4560–4567, https://doi.org/10.1103/PhysRevB.7.4560.

[18] H. Sumiya, S. Satoh, High-pressure synthesis of high-purity diamond crystal, Diam. Relat. Mater. 5 (1996) 1359–1365, https://doi.org/10.1016/0925-9635(96)00559-6.

[19] A.S. Vishnevskii, A.G. Gontar, V.I. Torishnii, A.A. Shul'zhenko, Electrical conductivity of heavily doped p-type diamond, Sov. Phys. Semiconduct. 15 (1981) 659.

[20] A. Cięciwa, R. Wüthrich, C. Comninellis, Electrochemical characterization of mechanically implanted boron-doped diamond electrodes, Electrochem. Commun. 8 (2006) 375–382, https://doi.org/10.1016/j.elecom.2005.12.013.

[21] V.D. Blank, M.S. Kuznetsov, S.A. Nosukhin, S.A. Terentiev, V.N. Denisov, The influence of crystallization temperature and boron concentration in growth environment on its distribution in growth sectors of type IIb diamond, Diam. Relat. Mater. 16 (2007) 800–804, https://doi.org/10.1016/j.diamond.2006.12.010.

[22] B.N. Mavrin, V.N. Denisov, D.M. Popova, E.A. Skryleva, M.S. Kuznetsov, S.A. Nosukhin, S.A. Terentiev, V.D. Blank, Boron distribution in the subsurface region of heavily doped IIb type diamond, Phys. Lett. 372 (2008) 3914–3918, https://doi.org/10.1016/j.physleta.2008.02.064.

[23] E.A. Ekimov, V.A. Sidorov, A.V. Zoteev, J.B. Lebed, J.D. Thompson, S.M. Stishov, Structure and superconductivity of isotope-enriched boron-doped diamond, Sci. Technol. Adv. Mater. 9 (2008), 044210, https://doi.org/10.1088/1468-6996/9/4/044210.

[24] H.S. Li, Y.X. Qi, J.H. Gong, M. Wang, M.S. Li, High-pressure synthesis and characterization of thermal-stable boron-doped diamond single crystals, Int. J. Refract. Metals Hard Mater. 27 (2009) 564–570, https://doi.org/10.1016/j.ijrmhm.2008.07.015.

[25] F.M. Shakhov, A.M. Abyzov, S.V. Kidalov, A.A. Krasilin, E. Lähderanta, V.T. Lebedev, D.V. Shamshur, K. Takai, Boron-doped diamond synthesized at high-pressure and high-temperature with metal catalyst, J. Phys. Chem. Solid. 103 (2017) 224–237, https://doi.org/10.1016/j.jpcs.2016.11.020.

[26] M.E. Snowden, A.G. Güell, S.C.S. Lai, K. McKelvey, N. Ebejer, M.A. Oconnell, A.W. Colburn, P.R. Unwin, Scanning electrochemical cell microscopy: theory and experiment for quantitative high resolution spatially-resolved voltammetry and simultaneous ion-conductance measurements, Anal. Chem. 84 (2012) 2483–2491, https://doi.org/10.1021/ac203195h.

[27] H. Kanda, Crystal growth of diamond, in: Bulk Cryst. Growth Electron. Opt. Optoelectron. Mater, wiley, 2010, pp. 407–432, https://doi.org/10.1002/9780470012086.ch14.

[28] J. Lu, Z. Kou, T. Liu, X. Yan, F. Liu, W. Ding, Q. Zhang, L. Zhang, J. Liu, D. He, Submicron binderless polycrystalline diamond sintering under ultra-high pressure, Diam. Relat. Mater. 77 (2017) 41–45, https://doi.org/10.1016/j.diamond.2017.05.011.

[29] S. Osswald, G. Yushin, V. Mochalin, A. Sergei, O. Kucheyev, Yury gogotsi, control of sp2/sp3 carbon ratio and surface Chemistry of nanodiamond powders by selective oxidation in air, J. Am. Chem. Soc. 128 (2006) 11635–11642, https://doi.org/10.1021/JA063303N.

[30] C. Zhen, X. Liu, Z. Yan, H. Gong, Y. Wang, Characteristics of Au/Ti/p-diamond ohmic contacts prepared by r.f. sputtering, Surf. Interface Anal. 32 (2001) 106–109, https://doi.org/10.1002/sia.1017.

[31] G. Zhang, S. Tan, A.N. Patel, P.R. Unwin, Electrochemistry of $Fe^{3+/2+}$ at highly oriented pyrolytic graphite (Hopg) electrodes: kinetics, identification of major electroactive sites and time effects on the response, Phys. Chem. Chem. Phys. 18 (2016) 32387–32395, https://doi.org/10.1039/C6CP06472H.

[32] D.-Q. Liu, C.-H. Chen, D. Perry, G. West, S.J. Cobb, J.V. Macpherson, P.R. Unwin, Facet-Resolved electrochemistry of polycrystalline boron-doped diamond electrodes: microscopic factors determining the solvent window in aqueous potassium chloride solutions, ChemElectroChem 5 (2018) 3028–3035, https://doi.org/10.1002/celc.201800770.

[33] C.H. Chen, L. Jacobse, K. McKelvey, S.C.S. Lai, M.T.M. Koper, P.R. Unwin, Voltammetric scanning electrochemical cell microscopy: dynamic imaging of hydrazine electro-oxidation on platinum electrodes, Anal. Chem. 87 (2015) 5782–5789, https://doi.org/10.1021/acs.analchem.5b00988.

[34] D. Perry, D. Momotenko, R.A. Lazenby, M. Kang, P.R. Unwin, Characterization of nanopipettes, Anal. Chem. 88 (2016) 5523–5530, https://doi.org/10.1021/acs.analchem.6b01095.

[35] L.A. Hutton, J.G. Iacobini, E. Bitziou, R.B. Channon, M.E. Newton, J.V. Macpherson, Examination of the factors affecting the electrochemical performance of oxygen-terminated polycrystalline boron-doped diamond

electrodes, Anal. Chem. 85 (2013) 7230–7240, https://doi.org/10.1021/ac401042t.
[36] A.F. Khokhryakov, Y.N. Palyanov, Revealing of dislocations in diamond crystals by the selective etching method, J. Cryst. Growth 293 (2006) 469–474, https://doi.org/10.1016/j.jcrysgro.2006.05.044.
[37] J.C. Angus, T.J. Dyble, Etching models for A {111} diamond surface: calculation of trigon slopes, Surf. Sci. 50 (1975) 157–177, https://doi.org/10.1016/0039-6028(75)90180-6.
[38] A. Kromka, O. Babchenko, S. Potocky, B. Rezek, A. Sveshnikov, P. Demo, T. Izak, M. Varga, Diamond nucleation and seeding techniques for tissue regeneration, Diamond-Based Mater, Biomed. Appl. (2013) 206–255, https://doi.org/10.1533/9780857093516.2.206.
[39] S.J. Charles, J.W. Steeds, D.J.F. Evans, S. Lawson, J.E. Butler, Characterisation of electron irradiated boron-doped diamond, Diam. Relat. Mater. (2002), https://doi.org/10.1016/S0925-9635(01)00552-0.
[40] D. Waldorf, S. Liu, M. Stender, D. Norgan, Alternative binder carbide tools for machining superalloys, in: Proc. ASME Int. Manuf. Sci. Eng. Conf. MSEC2008, 2009, pp. 417–425, https://doi.org/10.1115/MSEC_ICMP2008-72369.
[41] Y.N. Palyanov, Y.M. Borzdov, A.F. Khokhryakov, I.N. Kupriyanov, A.G. Sokol, Effect of nitrogen impurity on diamond crystal growth processes, Cryst. Growth Des. 10 (2010) 3169–3175, https://doi.org/10.1021/cg100322p.
[42] A.M. Zaitsev, Optical Properties of Diamond, Springer Berlin Heidelberg, Berlin, Heidelberg, 2001, https://doi.org/10.1007/978-3-662-04548-0.
[43] M. Bernard, C. Baron, A. Deneuville, About the origin of the low wave number structures of the Raman spectra of heavily boron doped diamond films, Diam. Relat. Mater. 13 (2004) 896–899, https://doi.org/10.1016/j.diamond.2003.11.082.
[44] P. Gonon, E. Gheeraert, A. Deneuville, F. Fontaine, L. Abello, G. Lucazeau, Characterization of heavily B-doped polycrystalline diamond films using Raman spectroscopy and electron spin resonance, J. Appl. Phys. 78 (1995) 7059, https://doi.org/10.1063/1.360410.
[45] A.F. Azevedo, R.C. Mendes de Barros, S.H.P. Serrano, N.G. Ferreira, SEM and Raman analysis of boron-doped diamond coating on spherical textured substrates, Surf. Coating. Technol. 200 (2006) 5973–5977, https://doi.org/10.1016/j.surfcoat.2005.09.012.
[46] P. Szirmai, T. Pichler, O.A. Williams, S. Mandal, C. Bäuerle, F. Simon, A detailed analysis of the Raman spectra in superconducting boron doped nanocrystalline diamond, Phys. Status Solidi 249 (2012) 2656–2659, https://doi.org/10.1002/pssb.201200461.
[47] D. Kumar, M. Chandran, M.S. Ramachandra Rao, Effect of boron doping on first-order Raman scattering in superconducting boron doped diamond films, Appl. Phys. Lett. 110 (2017), 191602, https://doi.org/10.1063/1.4982591.
[48] A.C. Ferrari, J.C. Meyer, V. Scardaci, C. Casiraghi, M. Lazzeri, F. Mauri, S. Piscanec, D. Jiang, K.S. Novoselov, S. Roth, A.K. Geim, Raman spectrum of graphene and graphene layers, Phys. Rev. Lett. 97 (2006), 187401, https://doi.org/10.1103/PhysRevLett.97.187401.
[49] S. Yu, N. Yang, H. Zhuang, J. Meyer, S. Mandal, O.A. Williams, I. Lilge, H. Schönherr, X. Jiang, Electrochemical supercapacitors from diamond, J. Phys. Chem. C 119 (2015) 18918–18926, https://doi.org/10.1021/acs.jpcc.5b04719.
[50] E. Frackowiak, Carbon materials for supercapacitor application, Phys. Chem. Chem. Phys. 9 (2007) 1774, https://doi.org/10.1039/b618139m.
[51] D.A. Walsh, J.L. Fernández, J. Mauzeroll, A.J. Bard, Scanning electrochemical microscopy. 55. Fabrication and characterization of micropipet probes, Anal. Chem. 77 (2005) 5182–5188, https://doi.org/10.1021/ac0505122.
[52] D.P. Burt, N.R. Wilson, J.M.R.R. Weaver, P.S. Dobson, J.V. Macpherson, Nanowire probes for high resolution combined scanning electrochemical microscopy - atomic force microscopy, Nano Lett. 5 (2005) 639–643, https://doi.org/10.1021/nl050018d.
[53] B.D.B. Aaronson, C.H. Chen, H. Li, M.T.M. Koper, S.C.S. Lai, P.R. Unwin, Pseudo-single-crystal electrochemistry on polycrystalline electrodes: visualizing activity at grains and grain boundaries on platinum for the Fe 2+/Fe3+ redox reaction, J. Am. Chem. Soc. 135 (2013) 3873–3880, https://doi.org/10.1021/ja310632k.
[54] R. Bourne, ImageJ, in: Fundam. Digit. Imaging Med, 2010, https://doi.org/10.1007/978-1-84882-087-6_9.
[55] A. Bard, L. Faulkner, Electrochemical Methods: Fundamentals and Applications, second ed., 1944, https://doi.org/10.1016/B978-0-12-381373-2.00056-9.
[56] J.V. Macpherson, D. O'Hare, P.R. Unwin, C.P. Winlove, Quantitative spatially resolved measurements of mass transfer through laryngeal cartilage, Biophys. J. 73 (1997) 2771–2781, https://doi.org/10.1016/S0006-3495(97)78306-1.
[57] Y. Saito, A theoretical study on the diffusion current at the stationary electrodes of circular and narrow band types, Rev. Polarogr. 15 (1968) 177–187, https://doi.org/10.5189/revpolarography.15.177.
[58] J. Tomeš, Polarographic studies with the dropping mercury kathode. LXIII. Verification of the equation of the polarographic wave in the reversible electrodeposition of free kations, Collect. Czech Chem. Commun. 9 (1937) 12–21, https://doi.org/10.1135/cccc19370012.
[59] R.G. Compton, P.R. Unwin, Linear sweep voltammetry at channel electrodes, J. Electroanal. Chem. 206 (1986) 57–67, https://doi.org/10.1016/0022-0728(86)90256-1.